Theory-guided discovery of pressure-induced transitions in the fast-ion conductor BaSnF₄

Robin Turnbull , ^{1,*} Zhang YingLong , ² Claudio Cazorla , ^{3,4} Akun Liang , ^{1,5} Rahman Saqib , ² Miriam Peña-Alvarez , 6 Catalin Popescu , 7 Laura Pampillo , 8,9 and Daniel Errandonea 1 ¹MALTA Consolider Team, Departamento de Física Aplicada-ICMUV, Universidad de Valencia, 46100 Burjassot, Valencia, Spain ²School of Physics and Optoelectronic Engineering, Hangzhou Institute for Advanced Study, University of Chinese Academy of Sciences (UCAS), China ³Departament de Física, Universitat Politècnica de Catalunya, Campus Diagonal-Besòs, Av. Eduard Maristany 10-14, 08019 Barcelona, Spain ⁴Barcelona Research Center in Multiscale Science and Engineering, Universitat Politècnica de Catalunya, Campus Diagonal-Besòs, Av. Eduard Maristany 10-14, 08019 Barcelona, Spain ⁵Eastern Institute of Technology, Ningbo 315200, China ⁶Centre for Science at Extreme Conditions and School of Physics and Astronomy, University of Edinburgh, Edingurgh, EH9 3FD Scotland, United Kingdom ⁷CELLS-ALBA Synchrotron Light Facility, Cerdanyola, 08290 Barcelona, Spain ⁸ Facultad de Ingeniería, Laboratorio de Sólidos Amorfos, Universidad de Buenos Aires, Paseo Colón 850 (1063), Buenos Aires, Argentina ⁹Instituto de Tecnologías y Ciencias de la Ingeniería "Hilario Fernández Long" (INTECIN), CONICET-Universidad de Buenos Aires, Buenos Aires, Argentina

(Received 28 March 2025; revised 18 June 2025; accepted 22 September 2025; published 5 November 2025)

Fast-ion conductors such as $BaSnF_4$ are of significant interest for next-generation solid-state battery technologies due to their high ionic conductivity and chemical stability. However, the behavior of these materials under extreme conditions remains poorly understood, despite the relevance of pressure-induced modifications for tuning functional properties. In this study, we combine density functional theory (DFT) calculations with high-pressure experiments to investigate the structural evolution of $BaSnF_4$ up to 40 GPa. DFT predicts two pressure-induced phase transitions: from the ambient-pressure tetragonal P4/nmm phase to a monoclinic $P2_1/m$ -I structure at 10 GPa, and subsequently to a denser monoclinic $P2_1/m$ -II phase at 32 GPa. The first transition is experimentally confirmed via angle-dispersive X-ray diffraction, Raman spectroscopy, and electrical resistivity measurements, all performed at ambient temperature. The second transition is supported by distinct changes in high-pressure Raman modes and resistivity behavior, consistent with a further structural reorganization. These findings not only clarify the high-pressure phase diagram of $BaSnF_4$, but also shed light on the potential for pressure-tuned ionic transport in fluorostannate-based solid electrolytes.

DOI: 10.1103/sk37-q99z

I. INTRODUCTION

Fast-ion conductors are a class of solid-state materials that exhibit a sharp increase in ionic conductivity above a critical temperature [1]. Ion mobility is typically favored for small, monovalent ions, such as fluoride (F⁻), which are amongst the most mobile in the solid state. Fluoride-based materials with the fluorite structure type (MF $_2$, where M=Ba, Ca, Sr, Cd, Hg, Eu) are particularly well studied, with conductivities exceeding 0.1 S cm¹ at high temperatures [2]. These structures adopt the $Fm\bar{3}m$ space group and consist of a fcc metal lattice coordinated by eight fluoride ions, while the F⁻ ions occupy tetrahedral sites coordinated by four metal cations.

Published by the American Physical Society under the terms of the Creative Commons Attribution 4.0 International license. Further distribution of this work must maintain attribution to the author(s) and the published article's title, journal citation, and DOI.

Substituting a portion of the M^{2+} ions with $\mathrm{Sn^{2+}}$ leads to the formation of double-fluoride compounds with the formula $M\mathrm{SnF_4}$. These materials adopt derivatives of the fluorite structure with layered ordering of M and Sn cations, and exhibit significantly enhanced fluoride-ion conductivity, i.e., up to 3 orders of magnitude higher than the parent $M\mathrm{F_2}$ compounds [3]. Their relatively high conductivity, low cost, and absence of flammable liquid electrolytes make them promising candidates for solid-state fluoride-ion batteries, which are of increasing interest as alternatives to lithium-ion technology [4].

Despite their potential, the structural response of double fluorides to high pressure remains poorly understood. Pressure is known to influence ion transport by modifying the lattice dynamics and the local environment of mobile ions, with theoretical studies suggesting that it may reduce the superionic transition temperature in fluoride-based conductors [5,6]. Moreover, pressure-induced structural transitions in fast-ion conductors are of interest for solid-state cooling applications, where coupling between ionic conductivity and entropy changes may be exploited [7,8].

^{*}Contact author: robin.turnbull@uv.es

Here, we investigate the high-pressure behavior of BaSnF₄, a representative double-fluoride fast-ion conductor, using a combination of density functional theory (DFT) calculations and high-pressure experiments. Although BaSnF₄ is known to adopt a tetragonal structure (space group *P4/nmm*) at ambient conditions and exhibit good ionic conductivity, no experimental data exist regarding its behavior under compression. Our study aims to clarify the structural phase diagram of BaSnF₄ at high pressure and to assess the potential for pressure to influence its transport properties.

II. METHODS

A. Sample preparation

BaSnF₄ was prepared via a chemical coprecipitation synthesis method inspired by Ref. [9]. Stoichiometric amounts of barium chloride (BaCl₂) and stannous chloride (SnCl₂) were mixed together and dissolved in distilled water. This solution was then added dropwise into a solution of ammonium fluoride (NH₄F). The subsequent chemical reaction precipitates the final product, which is then filtered and dried:

$$BaCl_2 + SnCl_2 + 4NH_4F \rightarrow BaSnF_4 + 4NH_4Cl.$$

High-pressure angle-dispersive X-ray diffraction was measured using a diamond-anvil cell (DAC) with culets of 500 um in diameter. A 200-um-thick stainless steel sheet was used as a gasket material. It was indented to a thickness of 40 μm by the diamonds, and then a 150-μm hole was drilled in the center. An example sample loading is shown in Supplemental Material Fig. 1 [10]. The pressure medium was a mixture of methanol and ethanol in a 4:1 ratio [11]. Pressure was remotely controlled via a gas membrane. The experiment was performed at ALBA synchrotron on the BL04-MSPD beamline [12] using an X-ray wavelength of 0.4642 Å (26.7 keV) and beam size of approximately 20×20 µm FWHM. The x-ray diffraction (XRD) patterns were acquired on a Rayonix SX165 charged-coupled device (CCD) detector at a distance of 240.08 mm, using LaB₆ as a standard calibrant. Acquisition time was typically 30 s. The sample pressure was measured before and after XRD acquisition using the online ruby system of BL04. The two-dimensional (2D) diffraction images were integrated using dioptas [13] and Rietveld refinements were performed using profex [14].

High-pressure Raman spectra were acquired using the 514-nm emission line of an Ar^+ ion laser at around 25 mW. A Princeton Instruments Acton SpectraPro 2500i spectrometer was utilized, featuring interchangeable diffraction gratings with 300 and 1800 lines/mm. The CCD detector used for the Raman measurements was a Princeton Instruments model 7500-0003. Pressure was determined using the ruby fluorescence (<25 GPa) and diamond edge scales (>25 GPa) [15,16]. The Rayleigh scattering contribution to the spectrum is removed by passing the signal through two holographic notch filters. Helium was used as the pressure-transmitting medium and loaded into a piston-cylinder-type DAC equipped with 250- μ m culet diamonds and a rhenium gasket, which was indented to a thickness of 28 μ m with a 100- μ m diameter hole as the sample chamber.

High-pressure resistivity measurements were performed using the standard four-probe technique in a DAC with di-

amond culets of 300 µm in diameter. The sample resistivity was calculated according to the van der Pauw formula. A mixture of epoxy and cubic boron nitride was utilized as the coating on the steel gaskets to ensure electrical insulation between different electrodes. Four platinum electrodes and copper wires were set up to contact the sample in the chamber. No pressure medium was used for these measurements. Pressure was determined using the ruby scale.

B. Density functional calculations

First-principles calculations based on DFT [17] were carried out with the PBEsol exchange-correlation energy functional [18] as it is implemented in the VASP software [19]. The projector-augmented wave method [20] was employed to represent the ionic cores by considering the following electronic states as valence: Ba 5s5p6s; Sn 5s5p; F 2s2p. An energy cutoff of 750 eV and dense Monkhorst-Pack *k*-point densities (e.g., a 14×14×7 grid for the 12-atom bulk tetragonal unit cell) were used for integrations within the Brillouin zone, leading to total energies converged to within 1 meV per atom. Atomic relaxations were concluded when the forces in the atoms were all below 0.005 eV/Å. Phonon calculations were performed with the small-displacement method [21], using large 3×3×2 supercells containing a total of 216 atoms.

III. RESULTS AND DISCUSSION

A. Density functional theory calculations

Motivated by the lack of experimental studies on the high-pressure behavior of double fluorides, we performed DFT calculations on the double-fluoride BaSnF4 (barium tetrafluorostannate) in order to guide potential high-pressure experiments. Our DFT calculations predicted an ambienttemperature phase transition from the known ambientpressure fluorite-type tetragonal structure (P4/nmm) to a monoclinic structure $(P2_1/m-I)$ at just above P = 10 GPa. According to the DFT calculations, the tetragonal BaSnF₄ structure is vibrationally unstable at pressures higher than 22.1 GPa. In particular, we observe two Γ phonon modes exhibiting imaginary frequencies at such pressures, suggesting a dynamic instability that often precedes structural phase transition. Such vibrational instabilities are critical in fast-ion conductors, where structural rearrangements can alter ion migration pathways and impact ionic conductivity, as seen in similar fluoride systems [1,6]. The new low-enthalpy monoclinic phase in this work was determined by introducing the atomic displacements corresponding to one of the two Γ imaginary phonon modes in the unit cell of the tetragonal phase, and letting the system relax so as to minimize its energy. The tetragonal (P4/nmm) to monoclinic $(P2_1/m-I)$ phase transition is illustrated in the enthalpy plot in Fig. 2(a).

The calculated phonon spectrum of the high-pressure monoclinic $(P2_1/m\text{-I})$ BaSnF₄ structure, which confirms its predicted vibrational stability, is shown in Fig. 3(a) calculated at P=3 GPa. The predicted tetragonal to monoclinic transition was later confirmed experimentally in this work by high-pressure angle-dispersive synchrotron X-ray diffraction (HP-XRD; see next section). The calculated unit-cell parameters are compared to the experimentally

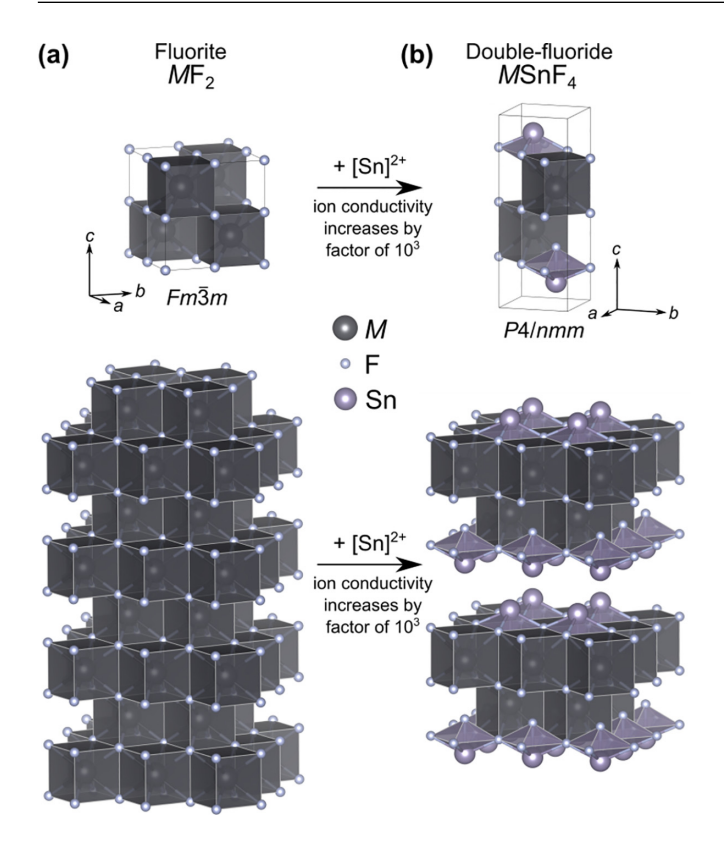


FIG. 1. (a) The fluorite (MF_2) structure. (b) The *double-fluoride* $(MSnF_4)$ structure.

determined unit-cell parameters from HP-XRD in the next section, showing good agreement. For the tetragonal phase, the maximum relative error occurs along the *c* axis at ambient pressure, reaching approximately 4%. As pressure increases, this error rapidly decreases to below 1%. In the monoclinic phase, the largest relative error is around 3%, observed at the highest applied pressure.

The DFT calculations also predicted a second pressureinduced phase transition from the aforementioned monoclinic $P2_1/m$ -I structure to a second monoclinic $P2_1/m$ -II structure, herein called monoclinic $P2_1/m$ -II, above P=32 GPa [see Fig. 2(b)]. This second low-enthalpy monoclinic phase was determined by considering the second of the two imaginary Γ phonon modes found for the tetragonal (P4/nmm) phase. While the lower pressure monoclinic $P2_1/m$ -I structure was confirmed by HP-XRD, XRD data have not been acquired at such high pressures, therefore the predicted $P2_1/m$ -II phase cannot be confirmed unambiguously in the present work. However, experimental high-pressure Raman spectra acquired up to P = 40 GPa (see Raman section) and resistivity measurements up to 56 GPa do indicate a possible phase transition around P = 30 GPa (see Section D. High-pressure Resistivity) in accordance with the DFT calculations.

To quantify the effect of the exchange-correlation functional on the DFT results, the two previously predicted phase transitions were recalculated using the PBE [22], RSCAN [23], and PBEsol-Sn(4d) functionals. The latter corresponds to the standard PBEsol functional, but includes the 4d orbitals of Sn in the valence configuration. As shown in Table I, the calculated transition pressures are consistent across all

TABLE I. Summary of the phase transition pressures calculated with different exchange functionals.

E_{xc} functional	$P4/nmm \rightarrow P2_1/m\text{-I (GPa)}$	$P2_1/m\text{-I} \rightarrow P2_1/m\text{-II (GPa)}$
PBEsol	10.3	32.5
PBEsol-Sn(4d)	10.3	33.5
PBE	13.9	36.4
RSCAN	11.7	36.4

cases, with particularly close agreement observed between the PBEsol and PBEsol-Sn(4d) results. The PBEsol functional was therefore used to perform most calculations in the present work because it is computationally affordable [especially compared to the PBEsol-Sn(4d) case] and has been shown to be especially good at predicting structural parameters of materials [24–26].

B. High-pressure angle-dispersive X-ray diffraction

To test the P4/nmm (ambient pressure) $\rightarrow P2_1/m$ -I (>10 GPa) hypothesis presented by the DFT calculations, we performed high-pressure angle-dispersive X-ray diffraction measurements on BaSnF₄. As a starting point, the ambient pressure BaSnF₄ XRD pattern was Rietveld refined using the tetragonal P4/nmm structure of Ref. [27] [see Fig. 4(c) for the crystal structure], confirming the published crystal structure and clearly showing a single phase sample [see Fig. 4(b)]. The difference between the observed and calculated intensities is shown by the gray line. The tetragonal BaSnF₄ structure is characterized by BaF₈ cubes and SnF₅E octahedra, where "E" represents the Sn lone electron pair (LEP), which points directly along the crystallographic c axis. Notably, the Sn LEP points towards the empty space between two Sn layers.

The P4/nmm tetragonal structure persisted as the only observable phase in subsequent XRD patterns acquired on compression until P=9.55 GPa, with the patterns exhibiting only shifting of reflections to higher 2\O values due to compression (i.e., smaller d spacings) within this pressure range. The unit-cell parameters determined from the XRD data during the compression phase are shown in Fig. 5(a). The c axis is clearly the most compressible, due to the high compressibility and alignment of the aforementioned Sn LEPs. According to the PASCal principal axis calculator [28], the c axis is the primary compression axis, exhibiting six times greater compressibility than the a or b axes. Over the studied pressure range, the tetragonal c axis contracts by 15.7%, whereas the a and b axes shrink by only 2.8%. The linear compressibility of the tetragonal a and b axes is 3.16 TPa¹, while that of the c axis is 18.05 TPa¹. For comparison, the linear compressibility of diamond is approximately 0.75 TPa¹.

Using these unit-cell parameters, we calculated the pressure-volume equation of state (EOS) for the low-pressure tetragonal phase, shown in Fig. 5(b). Fitting all of the volume data for the tetragonal structure yields a third-order Birch-Murnaghan EOS with a very low bulk modulus, $B_0 = 12(1)$ GPa, an exceptionally high bulk modulus

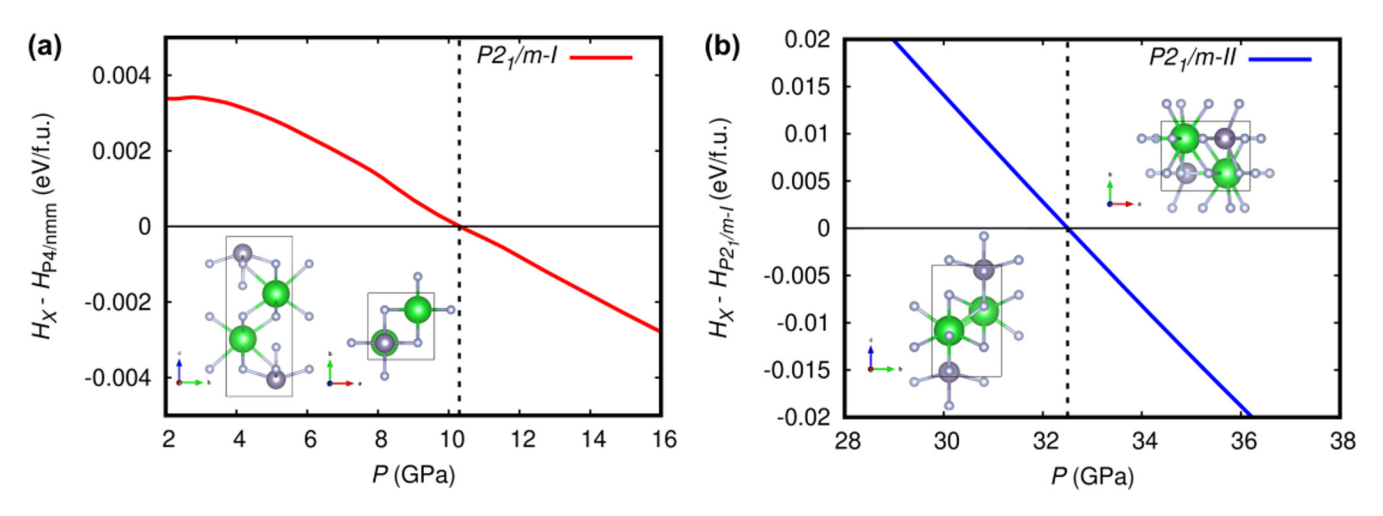


FIG. 2. (a) Calculated enthalpy of the high-pressure monoclinic $(P2_1/\text{m-I})$ BaSnF₄ structure relative to the ambient-pressure fluorite-type tetragonal structure (P4/nmm). (b) Calculated enthalpy of the higher-pressure monoclinic $(P2_1/\text{m-II})$ BaSnF₄ structure relative to the lower-pressure monoclinic $(P2_1/\text{m-I})$ BaSnF₄ structure of Fig. 1(a). The overall sequence of phase transitions predicted by DFT is P4/nmm (ambient pressure) $\rightarrow P2_1/\text{m-I}$ (>10 GPa) $\rightarrow P2_1/\text{m-II}$ (>32 GPa).

pressure derivative, B' = 16(1), and an initial volume of $V_0 = 216.5(5) \text{ Å}^3$.

The very low B_0 , comparable to that of solidified gases, suggests that this fit is unphysical. This underestimation of B_0 arises from the highly nonlinear compressibility of the c axis at pressures below 3 GPa. The high compressibility in this range is linked to the Sn lone electron pair, which points into the Sn-Sn interlayer region. For instance, the Sn-Sn interlayer distance decreases by 15% by a pressure of only P = 3 GPa [see Figs. 6(a) and 6(b)]. Consequently, the large B' reflects the significant interlayer compressibility due to the rapid reduction in Sn-Sn interlayer distances. Above 3 GPa the Sn-Sn interaction becomes more significant, as indicated by the change in slope of the c axis, reducing the compressibility. At 0 GPa the Sn-Sn interatomic distance is 4.33(2) Å. At 3.6 GPa the Sn-Sn interatomic distance is 3.80(2) Å. This is comparable to the next-nearest-neighbor Sn-Sn interatomic distance 3.767 69(0) Å in β -Sn at ambient pressure [29] shown in Fig. 6(c).

Additionally, the highly nonlinear compressibility of the c axis is underpinned by the pressure-induced evolution of the SnF₅ pyramid, as determined via Rietveld refinement of the experimental XRD data. As shown in the inset of Fig. 6(d), the SnF₅ unit consists of one short Sn-F bond and four longer, equivalent Sn-F bonds. The short bond is especially significant because it points along the c axis (the most compressible direction) and lies opposite the Sn LEP. The pressure dependence of the Sn-F bond lengths is illustrated in Fig. 6(d). While the four longer bonds (gray) remain largely unchanged with increasing pressure, the short Sn-F bond (red) exhibits more complex behavior. It first contracts rapidly from 2.1 to 1.8 Å between 0 and 1 GPa, but then, counterintuitively, it lengthens between 1 and 5 GPa. Similar anomalous bondlength increases under pressure have recently been observed in compounds containing IO₃ pyramids, attributed to the approach of next-nearest-neighbor atoms [30]. In the case of the SnF₅ pyramid, the four fluorine atoms from the adjacent Ba atom [located directly above or below, as shown in

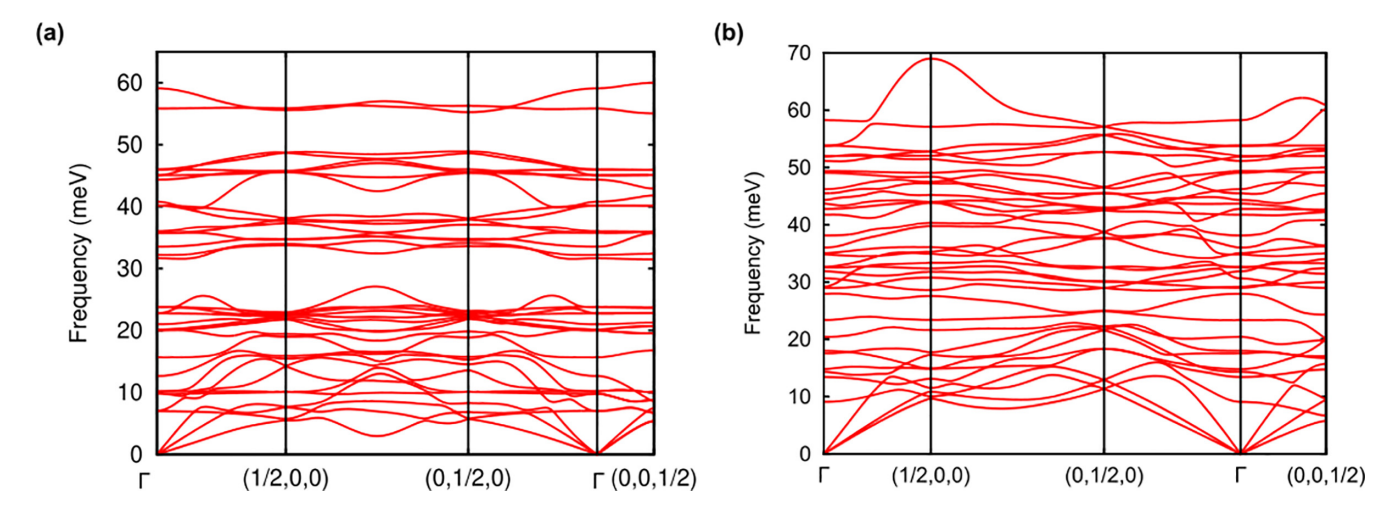


FIG. 3. Calculated phonon frequencies for (a) monoclinic $(P2_1/m\text{-I})$ BaSnF₄ at P = 11 GPa and (b) monoclinic $(P2_1/m\text{-II})$ BaSnF₄ at P = 34 GPa.

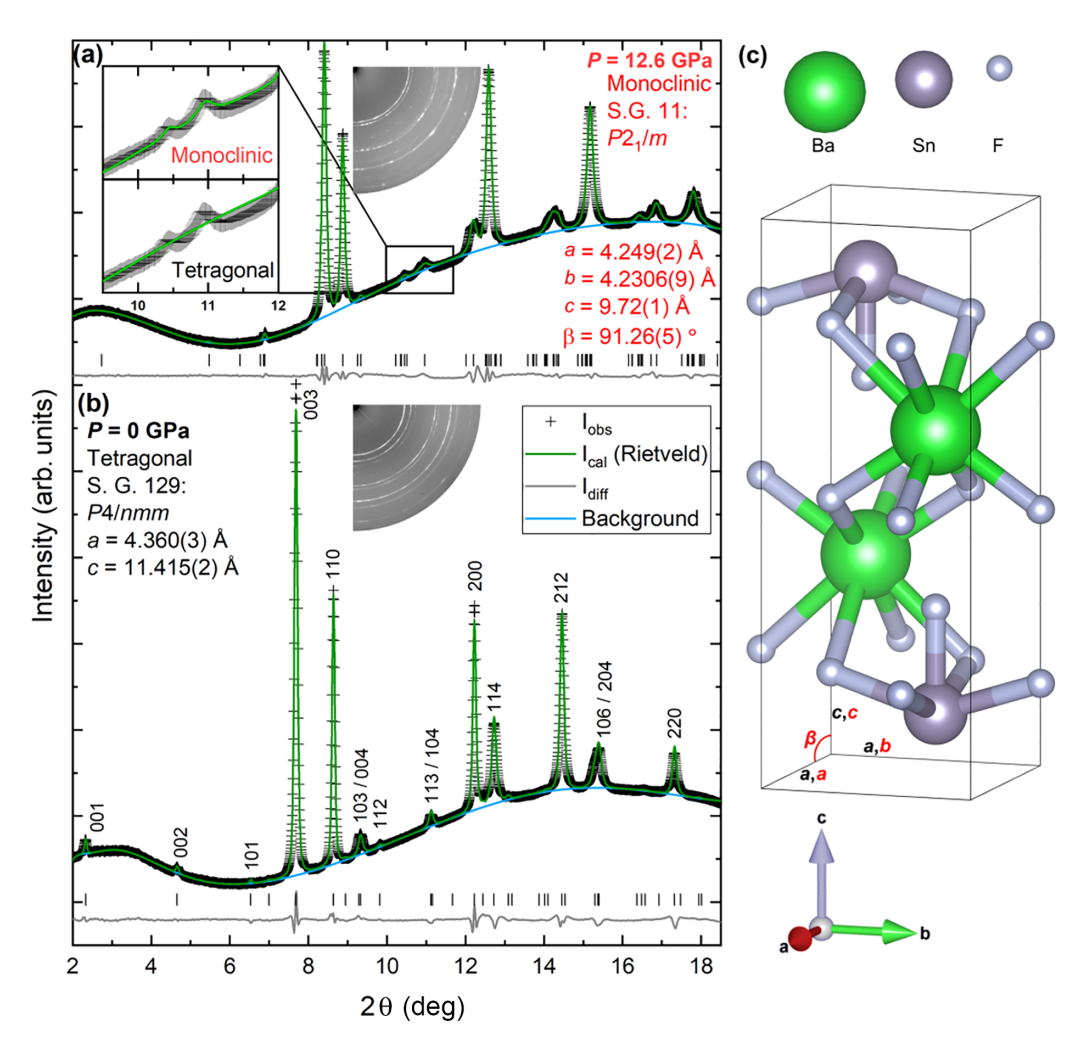


FIG. 4. Rietveld refinements of X-ray diffraction patterns from BaSnF₄ at (a) 12.6 GPa and (b) 0 GPa. The BaSnF₄ crystal structure is shown in (c), where the black (red) labels correspond to the tetragonal (monoclinic) structure. The experimentally observed intensity is shown with black crosses. The calculated intensity of the Rietveld profile is shown in green. The difference between the observed and calculated intensities is shown in gray. The background is shown in blue. The inset shows an enlarged image of the region 9.5° to 12°, where two low-intensity reflections are observed, which cannot be accounted for by the original tetragonal structure. The two reflections are accounted for by the monoclinic structure as shown in the inset. Vertical tick marks show the positions of the Bragg reflections, which are also labeled with their *hkls*. The insets show the unintegrated 2D diffraction images.

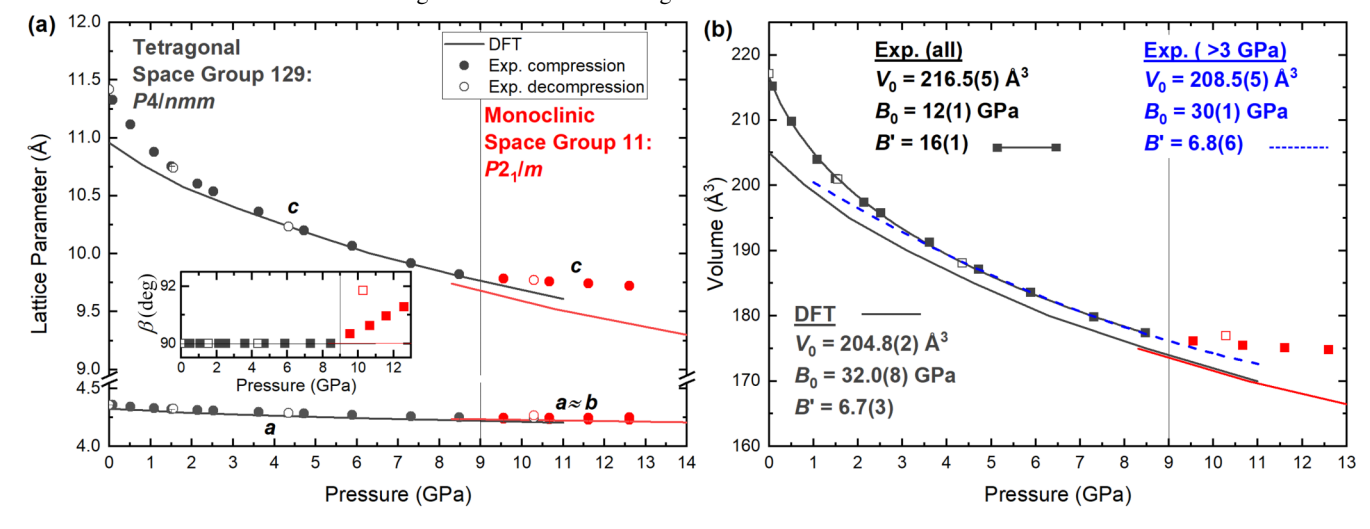


FIG. 5. (a) Experimental and calculated lattice parameters $(a, b, c, \text{ and } \beta)$ and (b) volume for the ambient-pressure tetragonal (P4/nmm) and high-pressure monoclinic $(P2_1/c)$ BaSnF₄ structures. The tetragonal BaSnF₄ data are shown in black. The monoclinic BaSnF₄ data are shown in red. Data acquired on (de)compression are shown with (open) solid symbols.

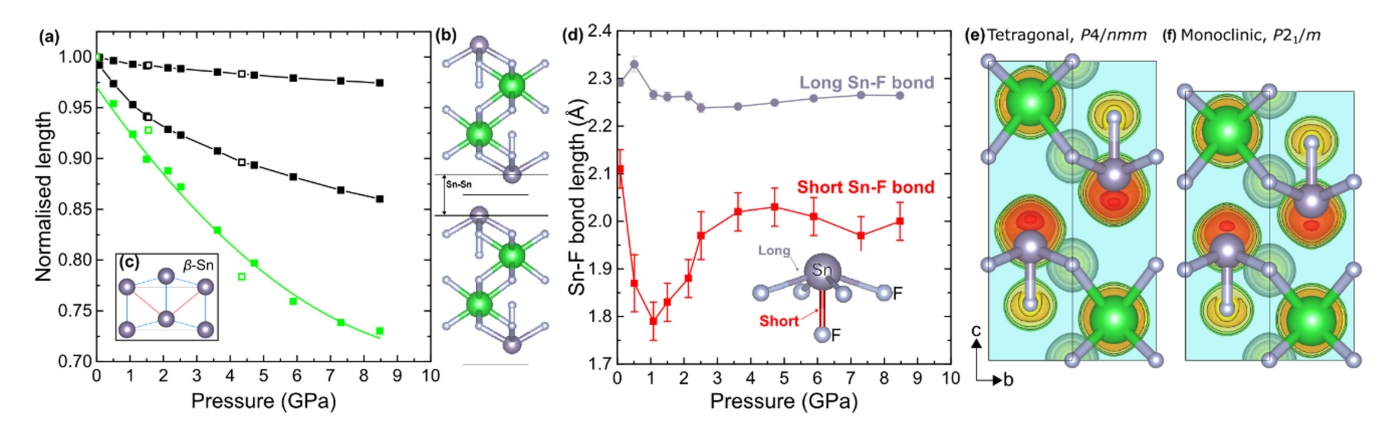


FIG. 6. (a) Normalized lengths of the unit-cell edges (a and c) and the Sn-Sn interlayer distance as indicated in (b). (c) The bc face of the β -Sn unit cell. Next-nearest-neighbor distances are shown with red lines. (d) The Sn-F bond lengths of the SnF₅ pyramid as determined from XRD. (e), (f) The (1, -1, 0) plane showing the electron localization function isosurfaces in the tetragonal and monoclinic-I BaSnF₄ phases.

Figs. 6(e) and 6(f)] move closer to the Sn atom under pressure, ultimately reaching a distance of 3.3 Å. This implies that the tetragonal-to-monoclinic phase transition in $BaSnF_4$ is accompanied by a coordination change around Sn, from fivefold to (5+4)-fold.

DFT calculations do not reproduce the highly compressible region below 3 GPa, likely due to the fact that DFT typically underestimates the ambient-pressure volume. In this work, the DFT volume at 0 GPa corresponds to the experimental volume at approximately 1.5 GPa. Shifting the DFT data empirically by this amount further improves the agreement between DFT and experiments.

To address the effect of the high compressibility below 3 GPa on the bulk modulus, a second EOS was calculated, excluding data below 3 GPa. This refinement yields a more reasonable bulk modulus pressure derivative, B' = 6.8(6), with $B_0 = 30(1)$ GPa and $V_0 = 208.5(5)$ Å³. The results from this revised EOS (using data above 3 GPa only) show excellent agreement with the EOS obtained from DFT-derived unit-cell parameters: $V_0 = 204.8(2)$ Å³, $B_0 = 32.0(8)$ GPa, and B' = 6.7(3). For comparison, the fluorite BaF₂ has a bulk modulus of $B_0 = 57$ GPa, and B' = 4 [31]. BaF₂ also exhibits a pressure-induced phase transition at the lower pressure of 3 GPa. Therefore, the introduction of Sn not only makes the structure more compressible, due to the empty layers between the Sn atoms, but it also increases the mechanostability.

Above P=9.55 GPa the Bragg reflections between 9.5° and 12° (shown in the inset in Fig. 4) cannot be accounted for by the original tetragonal P4/nmm symmetry, indicating a phase transition or chemical decomposition. All reflections are accounted for by the monoclinic $P2_1/m$ -I symmetry predicted by our DFT calculations as shown in the inset and in the upper panel of Fig. 4. This tetragonal \rightarrow monoclinic phase transition constitutes a slight distortion of the original tetragonal structure, wherein the unit-cell parameters that were initially a=b in the tetragonal case, become $a\approx b$ in the monoclinic case, with an angle β that deviates from 90° . The experimentally determined lattice parameters for the tetragonal P4/nmm and monoclinic $P2_1/m$ -I phases, along with the calculated lattice parameters for the tetragonal P4/nmm, monoclinic

 $P2_1/m$ -I, and monoclinic $P2_1/m$ -II phases, are provided in Supplemental Material Tables 1–5 [10]. The corresponding atomic positions are given in Supplemental Material Tables 6–10 [10]. While the overall phase evolution and transition pressures are in good agreement between experiment, DFT, Raman, and resistivity measurements, the slightly larger deviation in the experimentally observed β angle compared to DFT may arise from nonhydrostatic stress at high pressures in the experimental sample [32]. Such stress can cause uneven compression along different crystallographic axes, slightly distorting the crystal lattice. This effect is not captured in idealized (hydrostatic) DFT calculations.

The hypothesis of chemical decomposition can be excluded based on two key arguments. Firstly, there is excellent agreement between the calculated and experimental Raman spectra (see later, Fig. 7), whereas decomposition would typically yield new phases, such as SnF2 and BaF2, both known to be Raman active [33,34], with distinct vibrational modes. The absence of these characteristic modes in the experimental spectra strongly suggests that BaSnF4 has not decomposed. Secondly, the observed reversibility of the phase transition (as shown by the "recovered" diffraction pattern in Supplemental Material Fig. 2 [10]) indicates no permanent chemical change, since pressure-induced decomposition is typically irreversible at ambient temperature [35]. Additionally, the reaction between SnF₂ and BaF₂ to reform BaSnF₄ requires temperatures above 500 °C, while all measurements were conducted at ambient temperature [36].

C. High-pressure Raman Spectra

According to group-theoretical analysis, the tetragonal structure of BaSnF₄ has 12 Raman-active modes: $4A_{1g} + 2B_{1g} + 6E_g$. In the experimental spectra [see Fig. 7(a)], at ambient pressure we detected six Raman modes, and a broadband around 150 cm⁻¹, which we do not ascribe to the sample because it was not observable when measuring the sample outside the DAC environment (see Supplemental Material Fig. 3 [10]). Amongst the observed modes, the strongest are the low-frequency modes at 41 and 60 cm⁻¹ and the high-frequency mode at 467 cm⁻¹. We also detected three week modes at 227, 262, and 298 cm⁻¹. According to our

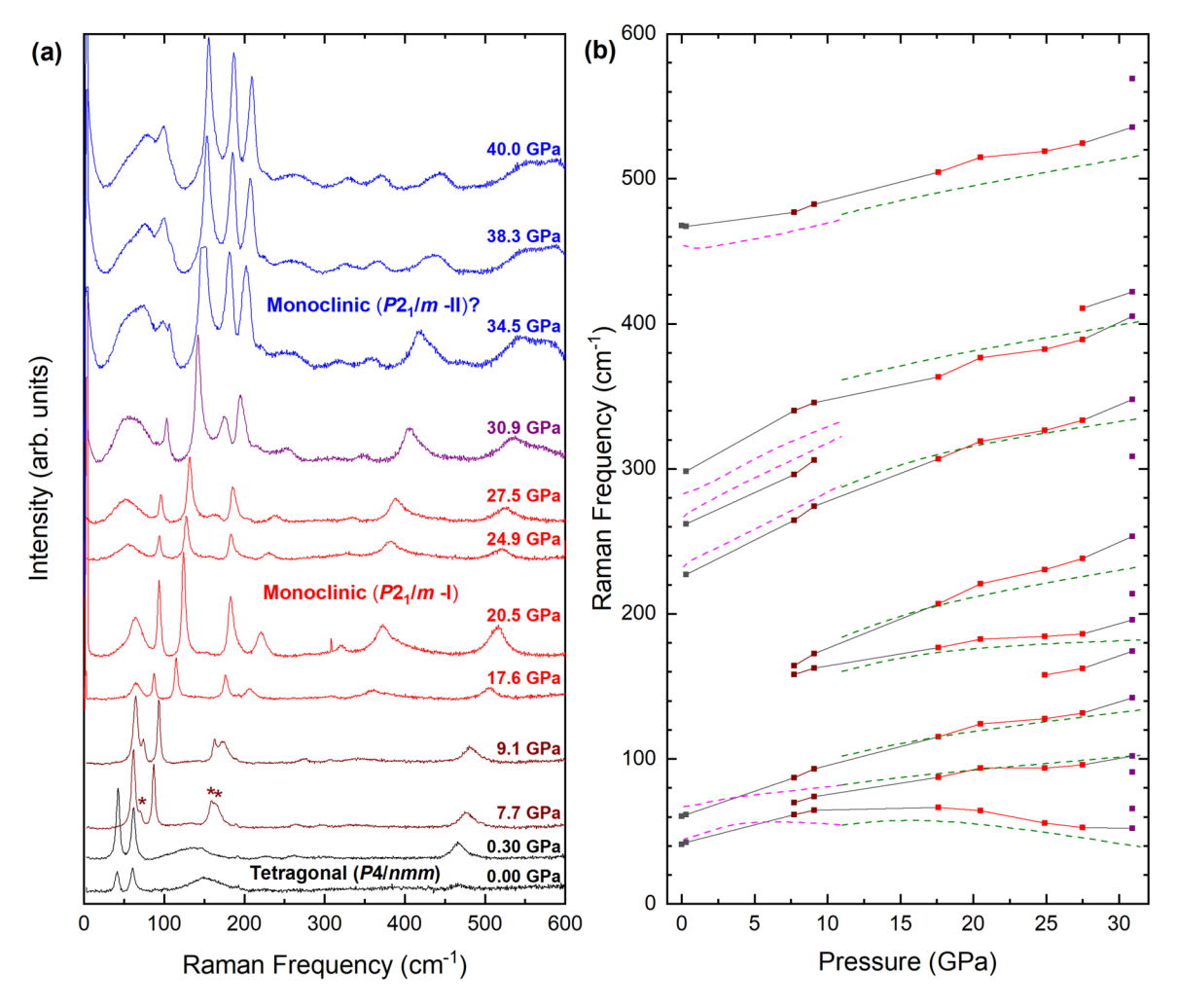


FIG. 7. Experimental and calculated high-pressure Raman data for BaSnF₄. (a) Experimental high-pressure Raman spectra. (b) Raman frequencies as a function of pressure. The experimental data corresponding to panel (a) are shown with symbols connected by solid lines. Calculated Raman modes are shown with dashed lines, where magenta and green correspond to the tetragonal (P4/nmm) and monoclinic ($P2_1/m$ -I) phases, respectively.

DFT calculations the wave numbers of these modes are 44, 67, 232, 267, 283, and 454 cm^{-1} . The agreement is quite good, with wave-number differences within 10%, which is typical for DFT calculations [37]. The agreement is good not only for the value of the wave number of the modes at 0 GPa, but also for its pressure dependence as shown in Fig. 7(b). From the DFT calculations, we find that the lowest-frequency mode, which corresponds to a mode with E_g symmetry, starts to soften under compression near the transition pressure. This mode involves vibrations of the Sn atoms within the a-b plane, i.e., within the layers that form the crystal structure. This softening is a precursor to the phase transition and indicates a weakening of the restoring force against the corresponding deformation [38]. This phenomenon is typical of a gradual reduction of symmetry from tetragonal to monoclinic [39] like the one reported here in the present work.

The tetragonal-to-monoclinic transition is identified in the Raman spectra by the appearance of three Raman modes at a pressure of P=7.7 GPa. These modes are seen as a shoulder appearing at 70 cm⁻¹ and a doublet at 160 cm⁻¹; they are all marked with asterisks "*" in Fig. 7(a). According to group-

theoretical analysis, the monoclinic structure of BaSnF₄ has 18 Raman-active modes: $12A_g + 6B_g$. In the experiments we detected up to ten Raman modes at 27.5 GPa. The increase in the number of modes is consistent with the phase transition from tetragonal to monoclinic. At 17.6 GPa, there are seven observed modes and they are at 66, 87, 115, 176, 207, $307, 363, \text{ and } 505 \text{ cm}^{-1}$. The calculated frequencies for these modes are 61, 90, 116, 176, 208, 313, 377, and 491 cm⁻¹. As in the case of the low-pressure tetragonal phase, the agreement between calculations and experiments is also good for the high-pressure phase, both for the values of calculated frequencies at 17.6 GPa and for the pressure dependence of the modes observed in experiments [see Fig. 7(b)]. An interesting observation is that the lowest-frequency mode observed in the HP phase softens under compression. This might be related to the occurrence of a second phase transition as predicted by DFT calculations. The occurrence of such transition is consistent with changes occurring in the Raman spectrum at 30.9 GPa. The predicted HP phase has also 18 Raman modes, $12A_{\circ}+6B_{\circ}$. Since the structure of this phase has yet to be confirmed by XRD, we prefer not to compare the pressure

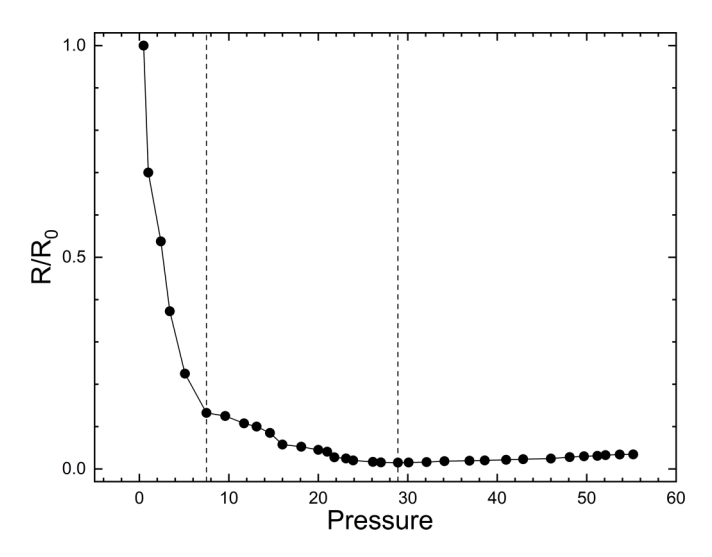


FIG. 8. Results of high-pressure resistivity measurements. Symbols are the results. The line is a guide to the eye. The vertical dashed lines indicate the transition pressures.

dependence of Raman modes of the second HP phase with results from DFT calculations.

D. High-pressure Resistivity

Figure 8 presents the results of high-pressure resistivity measurements. Initially, the resistivity decreases by an order of magnitude from 0 to 7.5 GPa, reaching $R/R_0 = 0.1325$. At 7.5 GPa, there is a change in the slope of the pressure dependence. The potential influence of initial packing effects, such as loosely packed grains or the collapse of voids, on the observed resistivity drop at low pressure has been considered. However, such effects are expected to be negligible above \sim 1–2 GPa, as any intergranular gaps would be fully closed within this pressure range [40]. Furthermore, the observed linear decrease in resistivity up to 7.5 GPa suggests a systematic, pressure-induced structural modification rather than a packing artifact. This interpretation is supported by complementary evidence from XRD, Raman spectroscopy, and DFT, all of which indicate a phase transition at similar but slightly higher pressures.

Beyond 7.5 GPa, the resistivity continues to decrease slightly with pressure, reaching a minimum of $R/R_0 = 0.015$ at 28.9 GPa, corresponding to a total decrease of two orders of magnitude from 0 GPa. Above 28.9 GPa, the resistivity begins to increase with pressure. The two changes in pressure dependence occur at pressures similar to the observed and predicted transition pressures, providing further evidence of these transitions. The resistivity measurements detect the transitions at slightly lower pressures because the experimental conditions were not hydrostatic.

The decrease in resistivity observed in the low-pressure tetragonal phase cannot be attributed to pressure-induced changes in band-gap energy, as fluorides have a wide band gap [41]. Instead, it is more likely due to a reduction in the activation energy for fluoride migration within the structure, which is 0.3 eV at 0 GPa [42]. A decrease of just 0.05 eV is sufficient to account for the observed change in resistivity. This change

TABLE II. Summary of the phase transition pressures observed in the different diagnostics and calculations in this work.

	Transition 1 (GPa) $P4/nmm \rightarrow P2_1/m$ -I	Transition 2 (GPa) $P2_1/m\text{-I} \rightarrow P2_1/m\text{-II}$
DFT	10.2	32.4
XRD	9.5	No data
Raman	7.7	27.5
Resistivity	7.5	28.9

is comparable to the effect of increasing the temperature to 500 K [42], which also enhances conductivity in a similar manner to compression. This suggests that pressure creates structural frameworks with connected low-barrier diffusion channels that facilitate fluoride migration.

The slower decrease in resistivity observed in the first highpressure monoclinic phase (7.5-28.9 GPa) suggests that the ion diffusion mechanism in this pressure range is less sensitive to compression than in the low-pressure phase. While we do not propose a specific diffusion mechanism in this work, similar behavior has been attributed in previous studies to the preferential alignment of crystallites along the c axis [42]. Such orientation may impede the reduction in ionic resistivity due to the predominantly two-dimensional nature of fluorideion diffusion in BaSnF₄. Finally, the increase in resistivity following the second phase transition may be related to partial occupancy of interstitial sites by fluoride ions, which has been associated with a reduction in ionic conductivity [43].

IV. CONCLUSIONS AND DISCUSSION

DFT calculations predict two pressure-induced structural phase transitions in the fast-ion conductor BaSnF₄. The first, from the ambient tetragonal P4/nmm phase to a monoclinic $P2_1/m$ -I structure at ~ 10 GPa, is confirmed by angle-dispersive X-ray diffraction at room temperature. This transition is also consistent with discontinuities observed in Raman spectra and electrical resistivity. A second transition, from $P2_1/m$ -I to a distinct monoclinic phase $(P2_1/m$ -II) at ~ 32 GPa, is supported by pressure-dependent Raman features and a marked change in resistivity behavior. These findings are summarized in Table II.

The phase transitions identified here indicate that $BaSnF_4$ undergoes meaningful structural reorganization under pressure with regard to the fluoride-ion environment. Notably, a reduction in resistivity by nearly 1 order of magnitude is observed in the low-pressure $P2_1/m$ -I phase. This suggests enhanced fluoride-ion mobility under compression, consistent with previous observations in single-fluoride materials such as CaF_2 , where pressure is known to lower the superionic transition temperature and increase ion transport [6].

Compared to other fast-ion fluorides, such as CaF₂, SrF₂, and BaF₂, where pressure-induced structural transitions have been observed [44], BaSnF₄ shows a similar trend but in a structurally more complex system due to the layered double-fluoride arrangement. The fact that BaSnF₄ maintains a monoclinic symmetry through both high-pressure phases, yet exhibits distinct spectroscopic and transport properties, suggests subtle changes in the local environment of fluo-

ride ions or the mobility pathways. This structural flexibility under compression could make BaSnF₄ and related materials promising candidates for pressure-tuned ionic conductors.

These results contribute to a broader understanding of how high pressure affects ion transport in complex fluoride materials. Future work should aim to probe the ionic transport mechanisms in the high-pressure phases directly, possibly using impedance spectroscopy under pressure or molecular dynamics simulations to quantify diffusion pathways. It would also be relevant to explore the BaSnF₄ phase diagram at high temperatures.

In summary, this study provides an experimental investigation of BaSnF₄ under pressure, revealing two pressure-induced phase transitions and a pressure-enhanced conductivity response. These findings underscore the potential of pressure as a tool to manipulate structural and transport properties in double-fluoride materials and open up further directions for research in solid-state ionics and high-pressure materials science.

ACKNOWLEDGMENTS

The authors thank Vitaliy Bilovol and Sergio Ferrari for their contribution to the synthesis of the sample. The authors acknowledge funding from the Spanish Ministerio de Ciencia e Innovación (MICINN) and the Agencia Estatal de Investigación (MCIN/AEI/10.13039/501100011033) under No. PID2022-138076NB-C41. This study is part of the Advanced Materials Program supported by MCIU with funding from NextGenerationEU (PRTR-C17.I1) and Generalitat Valenciana. R.T. acknowledges funding from the Generalitat Valenciana for Postdoctoral Fellowship No.

CIAPOS/2021/20 and also acknowledges financial support from the Spanish Ministerio de Ciencia e Innovacion through Project No. PID2021-125518NB-I00 financed by MCIN/AEI/10.13039/501100011033. C.C. acknowledges financial support from the Spanish Ministry of Science and Innovation through Grant No. MCIN/AEI/10.13039/501100011033, from the European Union European Regional Development Fund (ERDF) under Project No. PID2023-146623NB-I00, and through the "María de Maeztu" Program for Units of Excellence (CEX2023-001300-M), as well as from the Generalitat de Catalunya (Grant No. 2021SGR-00343). M.P.-A. acknowledges the support of the UKRI Future leaders fellowship MRC-MR/T043733/1. C.P. acknowledges financial support from the Spanish Ministerio de Ciencia e Innovacion through Project No. PID2021-125927NB-C21. L.P. acknowledges financial support from Agencia Nacional de Promoción Cientfica y Tecnológica under Project No. PICT 201-0364. D. E. acknowledges the support from Generalitat Valenciana under grants CIPROM/2021/075 and MFA/2022/007. The authors thank ALBA for providing beamtime under Experiment No. 2020074389.

DATA AVAILABILITY

The data that support the findings of this article are not publicly available upon publication because it is not technically feasible and/or the cost of preparing, depositing, and hosting the data would be prohibitive within the terms of this research project. The data are available from the authors upon reasonable request.

- [1] X. He, Y. Zhu, and Y. Mo, Origin of fast ion diffusion in superionic conductors, Nat. Commun. 8, 15893 (2017).
- [2] B. M. Voronin and S. V. Volkov, Ionic conductivity of fluorite type crystals CaF₂, SrF₂, BaF₂, and SrCl₂ at high temperatures, J. Phys. Chem. Solids 62, 1349 (2001).
- [3] G. Dénès, A. Muntasar, M. C. Madamba, and J. M. Parris, Tin (II)-containing fluoride ion conductors: How tin multiplies the fluoride ion conduction by up to three orders of magnitude, WIT Trans. Eng. Sci. 133, 167 (2021).
- [4] X. Lian and M. Salanne, Capturing the interactions in the BaSnF₄ ionic conductor: Comparison between a machinelearning potential and a polarizable force field, J. Chem. Phys. 159, 144 (2023).
- [5] A. K. Sagotra and C. Cazorla, Stress-mediated enhancement of ionic conductivity in fast-ion conductors, ACS Appl. Mater. Interfaces 9, 38773 (2017).
- [6] C. Cazorla and D. Errandonea, Superionicity and polymorphism in calcium fluoride at high pressure, Phys. Rev. Lett. 113, 235902 (2014).
- [7] C. Cazorla and D. Errandonea, Giant mechanocaloric effects in fluorite-structured superionic materials, Nano Lett. 16, 3124 (2016).
- [8] A. K. Sagotra, D. Errandonea, and C. Cazorla, Mechanocaloric effects in superionic thin films from atomistic simulations, Nat. Commun. 8, 963 (2017).

- [9] L. N. Patro and K. Hariharan, Influence of synthesis methodology on the ionic transport properties of BaSnF₄, Mater. Res. Bull. 46, 732 (2011).
- [10] See Supplemental Material at http://link.aps.org/supplemental/ 10.1103/sk37-q99z for figures and tables.
- [11] R. J. Angel, M. Bujak, J. Zhao, G. D. Gatta, and S. D. Jacobsen, Effective hydrostatic limits of pressure media for high-pressure crystallographic studies, J. Appl. Cryst. 40, 26 (2007).
- [12] F. Fauth, I. Peral, C. Popescu, and M. Knapp, The new material science powder diffraction beamline at ALBA synchrotron, Powder Diffr. 28, S360 (2013).
- [13] C. Prescher and V. B. Prakapenka, DIOPTAS: A program for reduction of two-dimensional X-ray diffraction data and data exploration, High Press. Res. 35, 223 (2015).
- [14] N. Doebelin and R. Kleeberg, *Profex*: A graphical user interface for the Rietveld refinement program *BGMN*, J. Appl. Cryst. 48, 1573 (2015).
- [15] G. Shen, Y. Wang, A. Dewaele, C. Wu, D. E. Fratanduono, J. Eggert, S. Klotz, K. F. Dziubek, P. Loubeyre, O. V. Fat'yanov, and P. D. Asimow, Toward an international practical pressure scale: A proposal for an IPPS ruby gauge (IPPS-Ruby2020), High Press. Res. 40, 299 (2020).
- [16] Y. Akahama and H. Kawamura, Pressure calibration of diamond anvil Raman gauge to 310 GPa, J. Appl. Phys. 100, 043516 (2006).

- [17] C. Cazorla and B. Boronat, Simulation and understanding of atomic and molecular quantum crystals, Rev. Mod. Phys. 89, 035003 (2017).
- [18] J. P. Perdew, A. Ruzsinszky, G. I. Csonka, O. A. Vydrov, G. E. Scuseria, L. A. Constantin, X. Zhou, and K. Burke, Restoring the density-gradient expansion for exchange in solids and surfaces, Phys. Rev. Lett. 100, 136406 (2008).
- [19] G. Kresse and J. Furthmüller, Efficient iterative schemes for ab initio total-energy calculations using a plane-wave basis set, Phys. Rev. B 54, 11169 (1996).
- [20] P. E. Blöchl, Projector augmented-wave method, Phys. Rev. B 50, 17953 (1994).
- [21] A. Togo, L. Chaput, T. Tadano, and I. Tanaka, Implementation strategies in phonopy and phono3py, J. Phys.: Condens. Matter 35, 353001 (2023).
- [22] J. P. Perdew, K. Burke, and M. Ernzerhof, Generalized gradient approximation made simple, Phys. Rev. Lett. **77**, 3865 (1996).
- [23] A. P. Bartók and J. R. Yates, Regularized SCAN functional, J. Chem. Phys. 150, 161101 (2019).
- [24] J. Schmidt, H.-C. Wang, T. F. T. Cerqueira, S. Botti, and M. A. L. Marques, A dataset of 175k stable and metastable materials calculated with the PBEsol and SCAN functionals, Sci. Data 9, 64 (2022).
- [25] G. I. Csonka, J. P. Perdew, A. Ruzsinszky, P. H. T. Philipsen, S. Lebègue, J. Paier, O. A. Vydrov, and J. G. Ángyán, Assessing the performance of recent density functionals for bulk solids, Phys. Rev. B 79, 155107 (2009).
- [26] F. Tran, J. Stelzl, and P. Blaha, Rungs 1 to 4 of DFT Jacob's ladder: Extensive test on the lattice constant, bulk modulus, and cohesive energy of solids, J. Chem. Phys. **144**, 204120 (2016).
- [27] M. M. Ahmad, Y. Yamane, and K. Yamada, Structure, ionic conduction, and giant dielectric properties of mechanochemically synthesized BaSnF₄, J. Appl. Phys. **106**, 074106 (2009).
- [28] M. J. Cliffe and A. L. Goodwin, *PASCal*: A principal axis strain calculator for thermal expansion and compressibility determination, J. Appl. Cryst. **45**, 1321 (2012).
- [29] J. A. Lee and G. V. Raynor, The lattice spacings of binary tinrich alloys, Proc. Phys. Soc. B **67**, 737 (1954).
- [30] A. Liang, R. Turnbull, C. Popescu, F. J. Manjón, E. Bandiello, P. Rodriguez-Hernandez, A. Muñoz, I. Yousef, Z. Hebboul, and D. Errandonea, Pressure-induced phase transition and increase of oxygen-iodine coordination in magnesium iodate, Phys. Rev. B 105, 054105 (2022).
- [31] J. M. Leger, J. Haines, A. Atouf, O. Schulte, and S. Hull, High-pressure x-ray-and neutron-diffraction studies of BaF₂: An example of a coordination number of 11 in *AX*₂ compounds, Phys. Rev. B **52**, 13247 (1995).

- [32] S. Klotz, J.-C. Chervin, P. Munsch, and G. Le Marchand, Hydrostatic limits of 11 pressure transmitting media, J. Phys. D: Appl. Phys. **42**, 075413 (2009).
- [33] T. Thomas, SnF₂-rich supercritical fluid in the Variscan tin deposit Zinnwald/Saxony, Germany, Geol. Earth Mar. Sci. 7, 1 (2025).
- [34] X. Zhang, L. Li, Y. Yu, Q. Zhang, N. Sun, Z. Mao, and D. Zhang, High pressure–temperature study of MgF₂, CaF₂, and BaF₂ by Raman spectroscopy: Phase transitions and vibrational properties of AF₂ difluorides, ACS Omega **9**, 23675 (2024).
- [35] E. Karaca, D. Santamaria-Perez, A. Otero-de-la-Roza, R. Oliva, K. S. Rao, S. N. Achary, C. Popescu, and D. Errandonea, Pressure-induced decomposition of Bi₁₄WO₂₄, Results Phys. 70, 108170 (2025).
- [36] G. Dénès, M. C. Madamba, and A. Muntasar, Reactivity of SnF₂ with fluorite type MF₂ versus M: Synthesis of high performance fluoride ion conductors, MRS Online Proc. Lib. 547, 377 (1998).
- [37] D. Errandonea, A. Muñoz, P. Rodríguez-Hernández, O. Gomis, S. N. Achary, C. Popescu, S. J. Patwe, and A. K. Tyagi, Highpressure crystal structure, lattice vibrations, and band structure of BiSbO₄, Inorg. Chem. 55, 4958 (2016).
- [38] A. Liang, S. Rahman, P. Rodríguez-Hernández, A. Muñoz, F. J. Manjón, G. Nenert, and D. Errandonea, High-pressure Raman study of Fe(IO₃)₃: Soft-mode behavior driven by coordination changes of iodine atoms, J. Phys. Chem. C **124**, 21329 (2020).
- [39] D. Errandonea and F. J. Manjón, On the ferroelastic nature of the scheelite-to-fergusonite phase transition in orthotungstates and orthomolybdates, Mater. Res. Bull. 44, 807 (2009).
- [40] C. R. Rotundu, T. Ćuk, R. L. Greene, Z. X. Shen, R. J. Hemley, and V. V. Struzhkin, High-pressure resistivity technique for quasi-hydrostatic compression experiments, Rev. Sci. Instrum. 84, 063903 (2013).
- [41] K. Suzuki, M. Cadatal-Raduban, M. Kase, and S. Ono, Band gap engineering of $Ca_xSr_{1-x}F_2$ and its application as filterless vacuum ultraviolet photodetectors with controllable spectral responses, Opt. Mater. **88**, 576 (2019).
- [42] G. Dénès, T. Birchall, M. Sayer, and M. F. Bell, BaSnF₄— A new fluoride ionic conductor with the α -PbSnF₄ structure, Solid State Ionics 13, 213 (1984).
- [43] B. Mercadier, C. Legein, M. Body, T. Famprikis, M. Morcrette, E. Suard, C. Masquelier, and D. Dambournet, Insights into the micro-structure-transport relationships of the fluoride-ion conductor *t*-BaSnF₄ synthesized by spark plasma sintering, Chem. Mater. **36**, 8076 (2024).
- [44] S. M. Dorfman, F. Jiang, Z. Mao, A. Kubo, Y. Meng, V. B. Prakapenka, and T. S. Duffy, Phase transitions and equations of state of alkaline earth fluorides CaF₂, SrF₂, and BaF₂ to Mbar pressures, Phys. Rev. B **81**, 174121 (2010).